Ref. Ares(2023)7420220 - 31/10/2023

Co-UDlabs

Building Collaborative Urban Drainage research Labs communities

D8.1. Report on determined Scalable Hydrodynamic Performance Protocols

Date of delivery - 31/10/2023

Authors: L. Cea, J. Anta, J. Naves, D. Carreres, E. Sañudo, M. Regueiro, J. Shucksmith, K. Brazier, A. Moreno-Rodenas

Institutions: University of A Coruña, University of Sheffield, Deltares

This project has received funding from the European Union's Horizon 2020 research and innovation programme under grant agreement N° 101008626

DOCUMENT TRACKS DETAILS

Project acronym	Co-UDlabs
Project title	Building Collaborative Urban Drainage research labs communities
Starting date	01.05.2021
Duration	48 months
Call identifier	H2020-INFRAIA-2020-1
Grant Agreement No	101008626

Deliverable Information	
Deliverable number	D8.1
Work package number	8
Deliverable title	Report on determined Scalable Hydrodynamic Performance Protocols of Task 8.1.1
Lead beneficiary	University of A Coruña
Authors	University of A Coruña (UDC) Luis Cea Jose Anta Juan Naves Daniel Carreres Esteban Sañudo Manuel Regueiro University of Sheffield (UoS) J. Shucksmith K. Brazier Deltares A. Moreno-Ródenas
Due date	31/10/2023
Actual submission date	31/10/2023
Type of deliverable	Report
Dissemination level	Public

VERSION MANAGEMENT

Revision history and quality check			
Version	Name	Date	Comment
V 0.1	Luis Cea (UDC)	01/07/2023	First draft
V 0.2	James Shucksmith, Kaeli Brazier (UoS)	27/07/2023	Contributions from UoS
V 0.3	Juan Naves, Daniel Carreres, Esteban Sañudo, Manuel Regueiro (UDC)	25/09/2023	Contributions from UDC
V 0.4	Luis Cea (UDC)	29/09/2023	Contributions from UDC and internal review
V 0.5	Antonio Moreno-Ródenas (Deltares)	26/10/2023	Contributions from Deltares
V1.0	Luis Cea, Juan Naves (UDC)	31/10/2023	Final version

All information in this document only reflects the author's view. The European Commission is not responsible for any use that may be made of the information it contains.

TABLE OF CONTENTS

LIST OF TABLES 4
LIST OF FIGURES 5
BACKGROUND: ABOUT THE CO-UDLABS PROJECT 6
LIST OF ACRONYMS 7
EXECUTIVE SUMMARY 8
1. INTRODUCTION 9
2. ANALYSIS AND ASSESSMENT OF NEW TECHNIQUES TO BUILD-UP THE TOPOGRAPHY/GEOMETRY OF URBAN DRAINAGE INFRASTRUCTURE WITH HIGH RESOLUTION 10
2.1. Experimental facilities surveyed 10
2.2. Elevation measurement techniques 10
2.3. 3D models results 12
2.4. Conclusions 15
3. REVIEW ON "OPTICAL IMAGING FOR PROCESS MONITORING IN URBAN DRAINAGE" 16
3.1. Key optical monitoring enabling technologies. 16
3.2. Scope of applications 17
4. APPLICATION OF IMAGING VELOCIMETRY TECHNIQUES FOR URBAN DRAINAGE APPLICATIONS 18
4.1. Installation of low-cost cameras 18
4.2. LSPIV methodology 19
4.3. Test procedure 21
4.4. Results 22
4.5. Conclusions 24
5. INVESTIGATING GEOMETRICAL EFFECTS ON HYDRAULIC ENERGY LOSSES DURING SEWER TO SURFACE FLOW INTERACTIONS DURING URBAN FLOODS 26
5.1. Introduction 26
5.2. Energy Loss Framework 26
5.3. Experimental setup 27
5.4. Results 29
5.5. Conclusion 31
6. CONCLUSIONS AND CONTRIBUTION TOWARDS THE OBJECTIVES OF CO-UDLABS 32
7. REFERENCES 33

List of tables

Table 2.1. Points surveyed for each studied model (BLOCK surface, BLOCK roof and STREET). 11
Table 2.2. Summary table with DEM fit to traditional topography using reference validation points for the three techniques (SfM, LiDAR and depth camera) and for each studied model (BLOCK surface, BLOCK roof and STREET) using RMSE as statistic. 15
Table 4.1: Details of the six grates used, from Rubinato et al (2018). 28
Table 4.2: Grate characteristics and liner fitting coefficients for each grate. 31

List of figures

Figure 2.1. a) Urban drainage BLOCK facility and surveyed area. b) STREET facility. 10

Figure 2.2: 3D models resulted from the three techniques (SfM, LiDAR and depth camera) for each studied model (BLOCK surface, BLOCK roof and STREET). Lidar was not able to measure on Street surface due to the black color of the permeable asphalt. 12

Figure 2.3: Comparison of DEM models obtained by the three techniques (SfM, LiDAR and depth camera) for each studied model (BLOCK surface, BLOCK roof and STREET) and compared with the traditional topographic survey. Dashed red lines indicate the profiles paths. Label units in meters. 13

Figure 2.4: Comparison of profiles obtained by the three techniques (SfM, LiDAR and depth camera) for each studied model (BLOCK surface, BLOCK roof and STREET) and compared with the conventional topographic survey. 14

Figure 3.1: Installation of cameras based on Raspberry Pi and lamps in BLOCK. Four positions distributed along the facility was selected to hold two different image acquisition systems and LED and UV lamps. 19

Figure 3.2: Calibration image with the chess pattern carpet disposed over the surface to get the real coordinates to rectify the frames. In addition, the result of the rectification over the calibration image is shown. 19

Figure 3.3: Example of the treatment of the frames including rectification of the recording projection, processing and filtering of the images recorded in order to highlight tracers and improve PIV cross-correlation results. The frame corresponds to the camera equipped with a picamera v2 at position A and the H3 experiment. 20

Figure 3.4: Example of postprocessing of raw vectors for H3 test using a raspberry equipped with the HQ camera placed on position A. 21

Figure 3.5: Tests carried out during the experimental campaign. 22

Figure 3.6: Velocity maps obtained in position A using the picamera and HQ camera configuration, respectively. The results correspond to steady conditions of test H2, which corresponds with the constant rain intensity of 50 mm/h. 22

Figure 3.7: Surface velocity maps obtained from HQ cameras at different times of test H3 corresponding with 5, 15, 71, 201 and 249 s from the start of a constant 80 mm/h 240 s rain. 23

Figure 3.8: Temporal variation of the mean velocities of an area of 0.3x0.3 m^2 (centered in coordinates X=9.65 m and Y=1.85 m following reference system of Figure 3.7) for HQ camera and picamera for experiments H1, H2, H3, which consist of constant 240 s rains (30,50 and 80 mm/h, respectively). 24

Figure 3.9: Temporal variation of the mean velocities of an area of 0.3x0.3 m^2 (centered in coordinates X=9.65 m and Y=1.85 m following reference system of Figure 3.7) for HQ camera and picamera for experiments H4, H5, H6. 24

Figure 4.1: Flows and head losses during surcharging pipe/overland flow interaction. 26

Figure 4.2: Diagram of the A/B rig structure (Beg et al. 2020). 28

Figure 4.3: Grates applied on top of manhole. Black arrows indicate the orientation of each grate. (Rubinato et al. 2018). 29

Figure 4.4: Plot of QE against Head in Pipe for all grate types. 30

Figure 4.5: Plot of the calculated energy loss coefficient from equation 2, against flow partition (Qe/Q3) for all grate types. 30

Background: about the Co-UDlabs Project

Co-UDlabs is an EU-funded project aiming to integrate research and innovation activities in the field of Urban Drainage Systems (UDS) to address pressing public health, flood risks and environmental challenges.

Bringing together 17 unique research facilities, Co-UDlabs offers training and free access to a wide range of high-level scientific instruments, smart monitoring technologies and digital water analysis tools for advancing knowledge and innovation in Urban drainage systems.

Co-UDlabs aims to create a urban drainage large-scale facilities network to provide opportunities for monitoring water quality, UDS performance and smart and open data approaches.

The main objective of the project is to provide a transnational multidisciplinary collaborative research infrastructure that will allow stakeholders, academic researchers, and innovators in the urban drainage water sector to come together, share ideas, co-produce project concepts and then benefit from access to top-class research infrastructures to develop, improve and demonstrate those concepts, thereby building a collaborative European Urban Drainage innovation community.

The initiative will facilitate the uptake of innovation in traditional buried pipe systems and newer green-blue infrastructure, with a focus on increasing the understanding of asset deterioration and improving system resilience.

List of acronyms

Acronym / Abbreviation	Meaning / Full text
CLAHE	Contrast Limited Adaptive Histogram Equalization
GPIO	General-purpose input/output
IMU	Inertial measurement unit
LiDAR	Laser Imaging Detection and Ranging
LSPIV	Large-Scale Particle Image Velocimetry
PIV	Particle Image Velocimetry
RMSE	Root mean squared error
SfM	Structure from Motion
UDS	Urban Drainage Systems

Executive summary

This document is Deliverable 8.1 of the Co-UDlabs project, funded under the European Union's Horizon 2020 research and innovation programme under grant agreement No 101008626. This deliverable is an output from Task 8.1.1 of Work Package 8 "Improving resilience and sustainability in urban drainage solutions".

The lead beneficiary of Work Package 8 is University of A Coruña, who is also the responsible partner for this Deliverable.

The Deliverable is a report on the main activities and results obtained within Task 8.1.1. Different innovative technologies and methodologies to analyze the hydrodynamic performance of urban drainage infrastructures were developed and tested in the laboratory, which also produced several experimental datasets. Special emphasis was put on the application of new optical and laser imaging techniques as Structure from Motion (SfM), Laser Imaging Detection and Ranging (LIDAR) or depth cameras, that are readily available within other fields but must still be adapted and tested on urban drainage infrastructures. These techniques can provide high resolution and accurate data that can be used for a better characterization of infrastructures as well as to estimate flow conditions as water depths or velocities under rainfall runoff conditions.

The geometrical effects on hydraulic energy losses during sewer to surface flow interactions has also been investigated in a specific activity due to the relevance of these flows during urban floods, which are therefore of paramount importance to improve our resilience to climate change.

1. Introduction

A comprehensive and accurate characterization of the hydrodynamics of urban flows is of paramount importance for a better design, management and adaption to climate change of urban drainage infrastructures. An effective adaption to climate change, which is expected to increase the number of extreme events in the future, needs a good understanding of the hydrodynamics of urban drainage flows. However, the complex geometry and flow patterns in urban environments makes difficult the measurement of water depths and velocities with a high resolution and accuracy. It is therefore of vital importance to develop new measurement protocols that take advantage of the currently available technologies. Specially interesting nowadays are image techniques, which can provide high resolution and comprehensive data at a relatively low cost and can be adapted to small-scale and large-scale conditions.

In this task we have worked in the application of new technologies to measure urban flows, with a special attention to imaging techniques. A review discussing the growing importance of optical measurements in urban drainage is being carried out involving several Co-UDlabs partners. It will explore various applications in urban drainage, including flow measurement, infrastructure mapping, and water quality monitoring and also address practical considerations for installing and maintaining optical sensors in this field. In addition, the deliverable shows how we have applied these techniques to experiments performed in large scale laboratory facilities. Structure from Motion, Laser Imaging Detection and Ranging or depth cameras were assessed to obtain high-resolution topographies, being this key to simulate in detail surface runoff in urban catchments. Imaging techniques can also be used to estimate water depths and velocities using LSPIV techniques with a high resolution and at a relatively low cost.

In addition, we have also dedicated a specific task to characterize the hydraulic energy losses during sewer to surface flow interactions during urban floods, in order to improve the current characterization of these kind of flooding.

2. Analysis and assessment of new techniques to build-up the topography/geometry of Urban Drainage infrastructure with high resolution

The quality of the results obtained in hydraulic numerical models is strongly conditioned by the accuracy of the input data, especially in the case of shallow waters such as those occurring in urban floods. In addition, urban catchments have kerbs and other urban elements, such as ditches or grates, that condition the flow of the runoff generated during an event. This also occurs in the case of laboratory studies in large-scale facilities, with traditional elevation measurement techniques being too time-consuming to obtain not very high-resolution topographies. Therefore, this work has analysed and evaluated three different devices and techniques to obtain accurate elevation maps with a high resolution: i) conventional camera with the Structure from Motion (SfM) photogrammetric technique, ii) Intel® RealSense™ LiDAR Camera L515 and iii) Depth camera Intel d435i. The measurements from cameras ii) and iii) were combined with a 3D reconstruction software. Finally, a topographic manual survey was used as a base for coordinate referencing and elevation comparison.

2.1. Experimental facilities surveyed

The study was carried out in the two urban drainage facilities STREET and BLOCK located at the Hydraulics Laboratory of the Centre of Technological Innovation in Construction and Civil Engineering (CITEEC), at University of A Coruña (Spain). The two facilities are being offered as part of the Transnational Access Co-UDlabs programme. The first facility named BLOCK consists of a T-intersection of two concrete streets considering 1:1 scale elements such as curbs, manholes and gully pots (Figure 2.1.a). This study was focused on an area of 20 m^2 (Figure 2.1.a) that covers the different types of elements present in the facility, including one of the roofs (henceforth Roof survey) and a fragment of surface including roadway, pathway, and drainage elements such as manholes and gratings (henceforth Surface survey). On the other hand, STREET facility consists of a 36 m^2 full-scale street section with a permeable asphalt as roadway (Figure 2.1.b). The two installations cover an interesting range of surfaces and textures to test the different methods and compare them with traditional manual surveying.

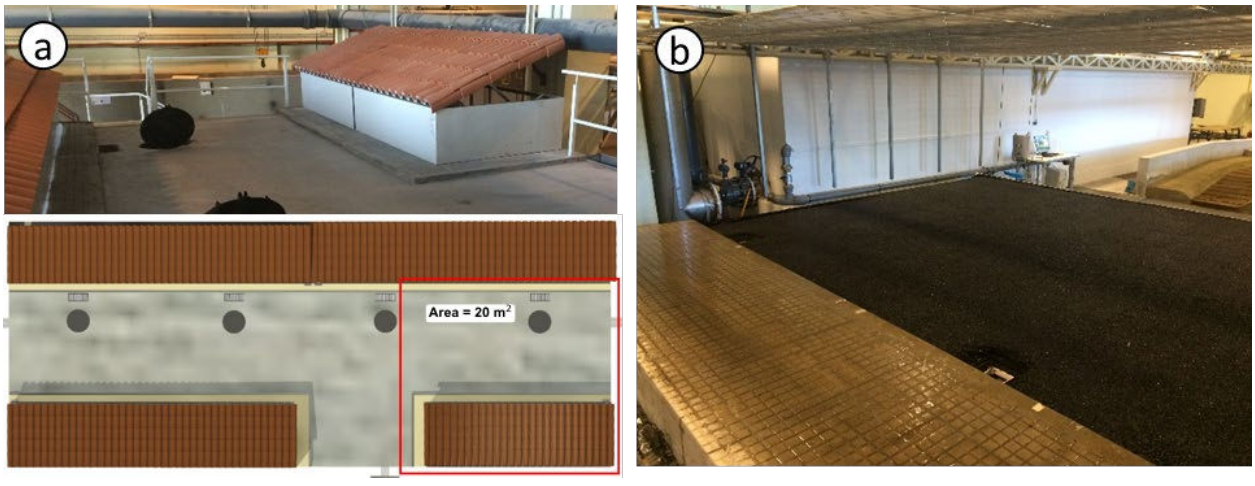

Figure 2.1. a) Urban drainage BLOCK facility and surveyed area. b) STREET facility.

2.2. Elevation measurement techniques

2.2.1. Topography survey

The XYZ coordinates of a grid of points marked at the different surfaces were obtained by a conventional topographic manual survey to be used as reference and validation points to compare the rest of techniques.

Elevations were measured point-by-point in each surface. The X and Y coordinates were obtained by relative distances between points, and the Z coordinate was obtained as the distance of the different points to a reference laser plane. Table 2.1 summarizes the number of points and the mean separation in each direction.

Part of the grid coordinates were used for the scaling and positioning of the topographies obtained by the LiDAR, depth camera and SFM techniques. The remaining validation points were used to assess the performance of the camera-based techniques.

Table 2.1. Points surveyed for each studied model (BLOCK surface, BLOCK roof and STREET).

	STREET	BLOCK Roof	BLOCK surface
Number of points	132	8	45
Mean spacing X-axis	0.5 m	0.3 m	0.7 m
Mean spacing Y-axis	0.5 m	0.2 m	0.5 m

2.2.2. Structure from Motion (SfM) photogrammetric technique

SfM is a computer vision technique used to reconstruct 3D structures from a collection of two-dimensional 2D images or photographs. By analyzing the patterns of visual features and their positions in multiple images taken from different viewpoints, SfM algorithms can estimate the 3D geometry of objects and scenes. The technique was used in this work to generate the 3D model of the BLOCK surface, the BLOCK roof, and the STREET facility surface. To do this, a series of images around each area were taken without any reference and with degrees of overlapping greater than 60% as recommended in the literature.

The VisualSfM software was used to process the images and reconstruct the 3D models resulting in a point cloud. In the case of the BLOCK facility, it was necessary projecting an image to introduce texture heterogeneity that allowed the software to obtain references to reconstruct the model (Figure 2.2). With the same purpose, some drawings were performed in the uniform asphalt black surface of the STREET facility. MeshLab software was then used to process these point clouds positioning and scaling by means of reference points with known coordinates (topography survey), and removing outliers. Finally, meshes were built using the Screened Poisson Surface Reconstruction function, which simplifies and smoothes the raw point clouds by fitting polynomial functions between the points.

2.2.3. Light Detection and Ranging (LiDAR)

The 3D LiDAR point clouds were obtained using the Intel® RealSense™ LiDAR Camera L515. LiDAR cameras capture simultaneously visual imagery and depth information, by sending out laser pulses and measuring their return time, offering a comprehensive view of the environment. The software RecFusion was simultaneously used to process the LiDAR data captured by the L515 sensor and reconstruct the 3D models.

The postprocessing of the reconstructed 3D models included the use of the built-in post-processing library OpenMesh: Mesh Decimation Framework to remove small-connected elements, cropping the mesh and specify the exported mesh size. Finally, the meshes were scaled and positioned using reference points of the topography survey using MeshLab software.

2.2.4. Depth Camera

The Intel RealSense Depth Camera D435i is an advanced depth-sensing camera that combines RGB imaging with accurate depth perception. Equipped with depth sensors and an inertial measurement unit (IMU), it captures detailed 3D depth maps and motion data simultaneously. The 3D reconstruction of the models was performed

through the software RecFusion and the postprocessing was carried out applying the same methodology as the data from LiDAR camera.

2.3. 3D models results

The 3D model reconstructions obtained for each of the methodologies and each of the areas are presented in Figure 2.2. The 3D reconstruction model of the STREET facility could not be obtained with the LiDAR camera because these cameras perform poorly in capturing surface with low reflectivity, such as black asphalt pavements. In this case, drawings failed to help in identifying the point cloud features with the LiDAR.

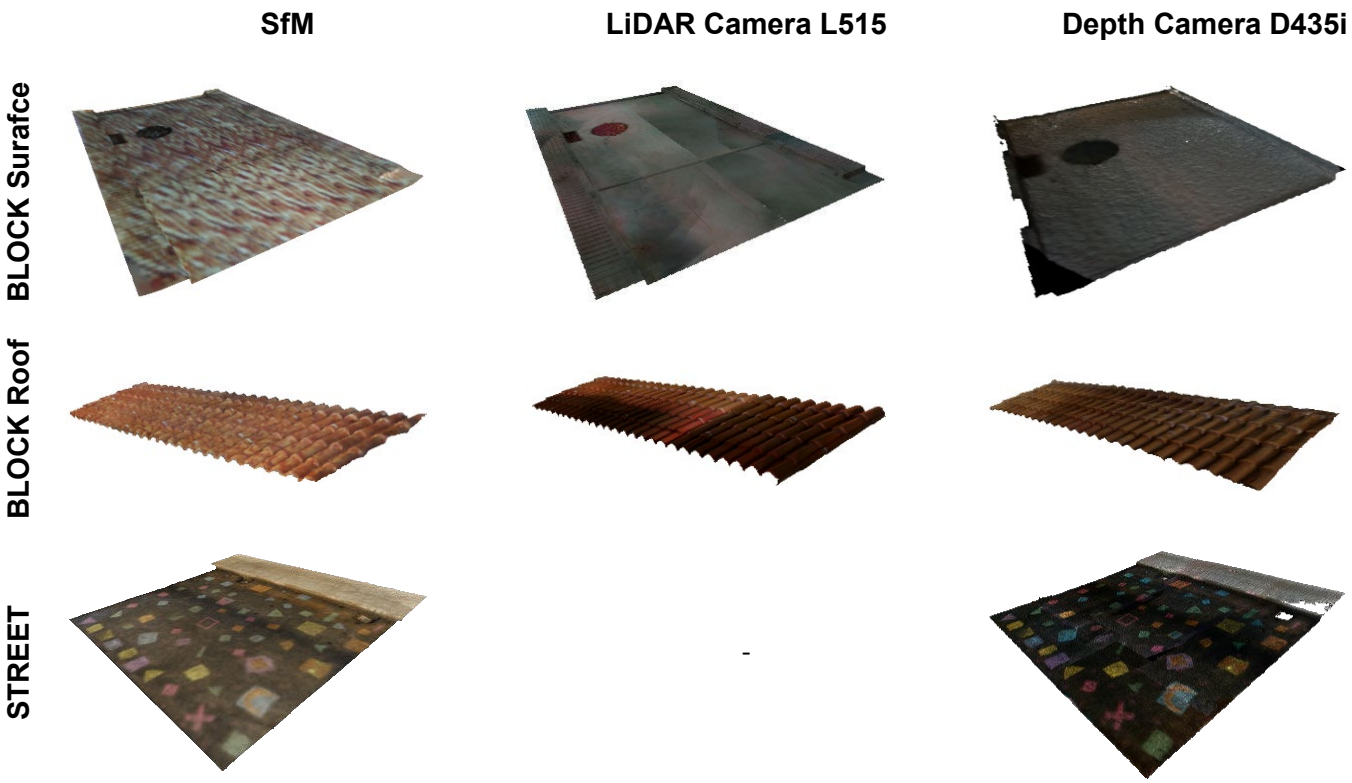

Figure 2.2: 3D models resulted from the three techniques (SfM, LiDAR and depth camera) for each studied model (BLOCK surface, BLOCK roof and STREET). Lidar was not able to measure on Street surface due to the black color of the permeable asphalt.

Figure 2.3 includes the elevation maps resulted from each technique (LiDAR, SfM, Depth camera and traditional topography) in the different surfaces (BLOCK surface, BLOCK roof and STREET). It can be seen how all the techniques have a good qualitative agreement with the conventional elevation survey, which indicates that adequate results were obtained with the scaling and processing of the model obtained. Main differences are observed in microscale topography since conventional topography does not consider small variations in the surface elevation, resulting in variations of centimeters compared to imaging techniques. The resolution needed for registering these variations with the conventional survey would be unaffordable in terms of work time and manpower, being this the main advantage found for imaging techniques against traditional methodologies. Nevertheless, absolute elevation references are required to be able to reference and scale the models reconstructed from the imaging techniques.

The LiDAR, SfM and depth camera showed variations even in a very flat area like the BLOCK surface (Figure 2.3). Similar trends were obtained in the other two surfaces, observing also signal noise introduced by the depth camera

for the STREET surface. It should be noted that LiDAR has not been able to measure the permeable asphalt surface of the STREET because of the black color of the surface even with the reference marks made.

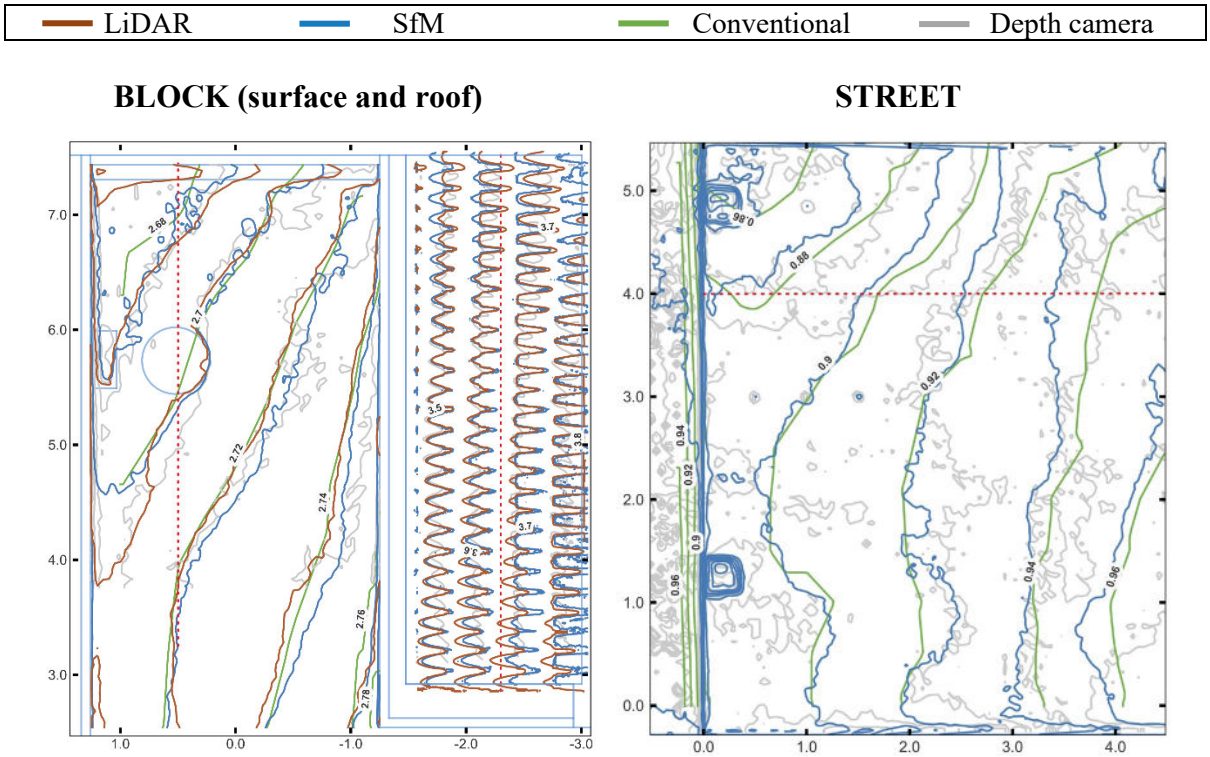

Figure 2.3: Comparison of DEM models obtained by the three techniques (SfM, LiDAR and depth camera) for each studied model (BLOCK surface, BLOCK roof and STREET) and compared with the traditional topographic survey. Dashed red lines indicate the profiles paths. Label units in meters

One cross section of each model is represented in Figure 2.4 to better interpret the results and validate the performance of the elevations compared to the topographic manual survey. Regarding the cross-section of the BLOCK surface, the SfM and LiDAR techniques were able to detect the small depression in the manhole cover that conventional topography was not able to record. The signal noise in the measurements obtained by the depth camera when recording the surface can also be observed. The same effect is also observed in the case of the STREET surface and could be related to the instantaneous reconstruction performed by the software RecFusion with the depth camera, which is generally prepared for static applications. Regarding the STREET roof, a good performance of the topographies is observed by fitting the shape of the roof tiles, with some small differences in the slopes of the models generated from the LiDAR and the SfM, being the depth camera the worst reconstruction model technique to detect the microscale topography of the tiles.

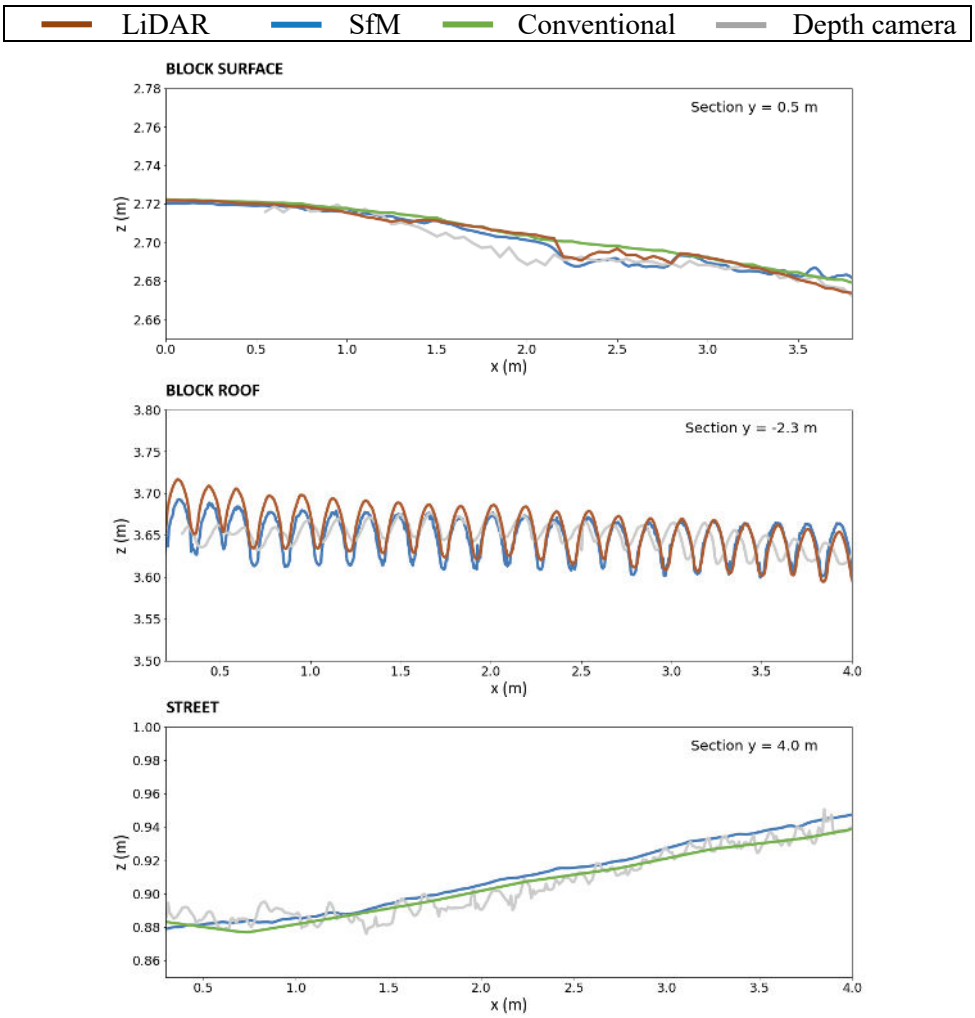

Figure 2.4: Comparison of profiles obtained by the three techniques (SfM, LiDAR and depth camera) for each studied model (BLOCK surface, BLOCK roof and STREET) and compared with the conventional topographic survey.

Finally, comparing the results obtained with validation points from topographic manual survey, an estimation of the error can be obtained to assess the performance of each technique. Root mean squared error (RMSE) between the elevations of validation points and the different 3D reconstructed models was selected as a comparison index. The performance observed in the elevation maps and corresponding cross-sections is shown in Table 2.2, being the SfM the technique with the best performance for all the cases. The topography obtained from LiDAR, also showed a good performance for BLOCK surface with a slightly high RMSE for the BLOCK roof due to the slope differences observed in the corresponding cross-section (Figure 2.4). Despite the noise introduced by the depth camera, the fit of the 3D reconstructed model to the validation points performed good for the flat surfaces of BLOCK and STREET. Therefore, more work in optimising the mesh postprocessing may be worthwhile to remove the noise, obtain more suitable results and, subsequently, present the depth camera as competitive as the rest of techniques. In case of the roof elevation map, the depth camera is not able to reproduce the microscale topography of the tiles and the RMSE is high.

Table 2.2. Summary table with DEM fit to traditional topography using reference validation points for the three techniques (SfM, LiDAR and depth camera) and for each studied model (BLOCK surface, BLOCK roof and STREET) using RMSE as statistic.

RMSE (mm)	**BLOCK surface**	**BLOCK roof**	**STREET**
SfM	4.0	4.3	4.0
LiDAR Camera L515	5.1	11.9	-
Depth Camera D435i	6.2	17.2	6.7

2.4. Conclusions

Three different techniques for obtaining accurate elevation maps with high resolutions were assessed in this work: i) conventional camera with the Structure from Motion (SfM) photogrammetric technique, ii) Intel® RealSense™ LiDAR Camera L515 and iii) Depth camera Intel d435i with a 3D reconstruction software. These methodologies were applied to three different surfaces corresponding to laboratory large-scale models of a concrete street and tiled roof. Elevation maps, cross sections and error estimations were analyzed for each combination of technique and surface and comparing it with a conventional topographic survey. Main differences are seen in microscale topography. While conventional topography is not considering small variations on the surface elevation, SfM and LiDAR are able to detect the small variations in the order of millimeters such us the depression due manholes. The depth camera 3D reconstructured model presented a significant noise in the elevation map, but the validating points indicate a good fit with conventional topographic survey that foster work towards improving the postprocessing of the raw data obtained. Regarding the tiled roof, the depth camera was not able to properly reproduce the shape of the tiles as LiDAR and SfM. Comparing the imaging techniques, SfM showed the best performance for all the cases. In addition, SfM present a low time and instrument costs, resulting in an optimal solution for obtaining a high-resolution and accurate elevation map in large-scale facilities.

3. Review on "Optical imaging for process monitoring in urban drainage"

Optical measurements represent an unvaluable source of data for water processes both in urban and natural environments. The last decade has witnessed a rapid growth of applications powered by technology enablers such as deep-learning, the reduction of optical sensors cost and the building of open-source software communities amongst others.

Within the JRA 8.1, the Co-uUDlabs partners are working towards a comprehensive review of optical measurement methods in the field of urban drainage. This review aims at identifying the state-of-the-art of optical hardware and processing techniques, compiling known applications in the urban drainage field, and discussing the outlook of field demands and techniques in the near future. This review is still underway, yet in this deliverable we summarize its main components.

3.1. Key optical monitoring enabling technologies.

Several technologies are fundamental for the implementation and popularization of image-processing techniques in field and laboratory applications in UD, this encompasses:

Hardware availability

This can be thought of as a combination of better affordability/accessibility to off-the-self hardware (e.g., standard CCTV solutions and laboratory equipment becoming cheaper and more accurate) to dedicated tailor-made optical sensing systems. For instance, programable micro-computer hardware in combination with high-quality sensors has resulted in the possibility of building fully tailored monitoring systems for under 100 Eur (e.g. Raspberry Pi + SONY 12-megapixel C-mount camera). Even recently, low-cost Global Shutter cameras (~50 Eur) promise better accessibility to tailor-made particle-image-velocimetry applications.

These factors have resulted in camera systems to be more ubiquitous (e.g., CCTV cameras in the urban environment), easier to access (i.e., democratization of sensing methods) and to deploy (less risk if vandalized / deterioration of field-deployed sensors).

Deep learning and image processing

Classical computer vision image-processing algorithms often rely on hand-tuned filters, thresholds levels (for instance when doing color-based filters). This is sometimes sufficient to do basic image processing (differentiate between surfaces in an image) or object detection (based on colors / geometry). However, these methods are typically highly sensitive to changes in light and require very controlled environments (typically only available under laboratory conditions). Thus, field implementations of optical monitoring have historically been challenging. With the introduction of Neural-Network based deep-learning processing routines, the generalization of vision models to different conditions (lighting, subjects, presence of occlusions or weather) is now possible. This has significantly enhanced the robustness of field-deployed measurement solutions.

Additionally, these models (deep-learning vision models) also provide auxiliary techniques that result in more flexible measurement solutions, such as: i) Image sharpening methods (super-resolution), ii) Noise reduction (e.g. mitigating light reflections, sensor noise and atmospheric occlusions like rain drops), geometrical extraction (water level and surfaces descriptions) and easily trainable object detection routines.

Open-source image processing communities

Beyond the large leaps in hardware and image processing techniques, a key factor in the expansion of optical monitoring applications has been the better accessibility to knowledge and software implementations. A large contribution to this comes from the creation of extensive open-software communities that allow collaboratively developing software. For instance, the community of OpenCV (Bradski, 2000) – a C++ / Python library for general computer vision applications – has been a cornerstone for the computer vision community. Another example can be found on OpenPIV (Liberzon et al., 2022) in the field of optical velocimetry-based applications, or TensorFlow (TensorFlow Developers 2023) which provides an extensive framework for the creation of deep-learning network architectures and training routines.

3.2. Scope of applications

Within the review paper we focus on optical monitoring methods for Urban drainage applications. This includes:

- Measurement of flows: Applications in the field and laboratory conditions of Particle-image velocimetry, Particle-Tracking velocimetry, Optical flow and the reconstruction of water levels and water flows around hydraulic structures.
- Optically based mapping and inspection of urban water infrastructure: Such as applications of Structure-from-motion, 3D stereo models and CCTV based asset status assessment.
- Water Quality: Focusing of multi-spectral (visible, infrared, Thermal) optical applications to monitor water quality dynamics.

Additionally, the review focuses on practical aspects for the installation, operation, and maintenance of optical sensors in UD. This is essential, since protocols for lighting, maintenance, data transfer or camera calibration are still largely unstandardized.

In this Deliverable, we advance some examples from the Co-UDlabs implementations, such as developments on velocity measurements or 3D reconstruction of structures. In the Co-UDlabs Review of optically based monitoring we focus on all implementations of interest known and relevant to the UD community, additionally we will discuss the developments most urgently required in the field from a technical and organizational perspective.

4. Application of imaging velocimetry techniques for urban drainage applications

Computer vision analyses digital images or videos to obtain high-level knowledge and perform tasks of the human visual system in an automatic way. Velocimetry is one of the possible applications of imaging techniques in urban drainage, being especially useful in laboratory experiments where velocity is a key variable characterizing certain phenomenon. Specifically, Particle Image Velocimetry (PIV) is a non-intrusive technique for obtaining 2D velocity maps that is commonly used in laboratory. PIV computes the movement of particles seeded in the flow, which are assumed to follow the same velocity, by using cross-correlation algorithms in two consecutive images with a certain time step between them. Large-scale PIV (LSPIV) is a variant of this technique which uses the flow surface as measurement plane, so it can be more easily applied to large-scale studies as the study area can be larger and expensive equipment such as complex lasers or cameras are no longer.

In this work, carried out within the scope of Joint Research Activity 3 (WP8), we have addressed the installation of a camera system to determine the velocities of runoff generated in the BLOCK rainfall simulator located at the Universidade da Coruña. This facility is being offered in the transnational access program of the Co-UDlabs project. The objective was to develop a methodology that allows for the measurement of velocities, complementing the hydraulic characterization of surface flow in the experiments conducted at the facility, as is the case with the hosted TA project (UDC-02-BLOCK-Zafra). This has enhanced the capabilities of the installation for internal and external users.

4.1. Installation of low-cost cameras

Raspberry Pi units have been employed in the context of video recording and processing. Beyond their affordability, these compact, single-board computers are recognized for their open architecture and flexibility. They are equipped with a Camera Serial Interface port for camera module attachment through a ribbon cable and a range of general-purpose input/output (GPIO) pins. Furthermore, they offer the convenience of remote control via their integrated Wi-Fi connectivity. Here, two different configurations were used: i) four Raspberry Pi 4B paired with an HQ Camera Module and ii) four Raspberry Pi Zero W paired with a v2 Camera Module. A total of 4 installation points (A, B, C and D in Figure 3.1) has been established to cover the full facility. Each point consists of 2 LED lamps and 2 UV lamps connected through GPIO to a Raspberry Pi 4, which has an HQ Camera. Additionally, a Raspberry Pi Zero W paired with a v2 Camera Module is also installed at each point to have a wider frame of the surface. All the raspberries were connected through WIFI to a central computer that can control the image acquisition and lighting of the installation.

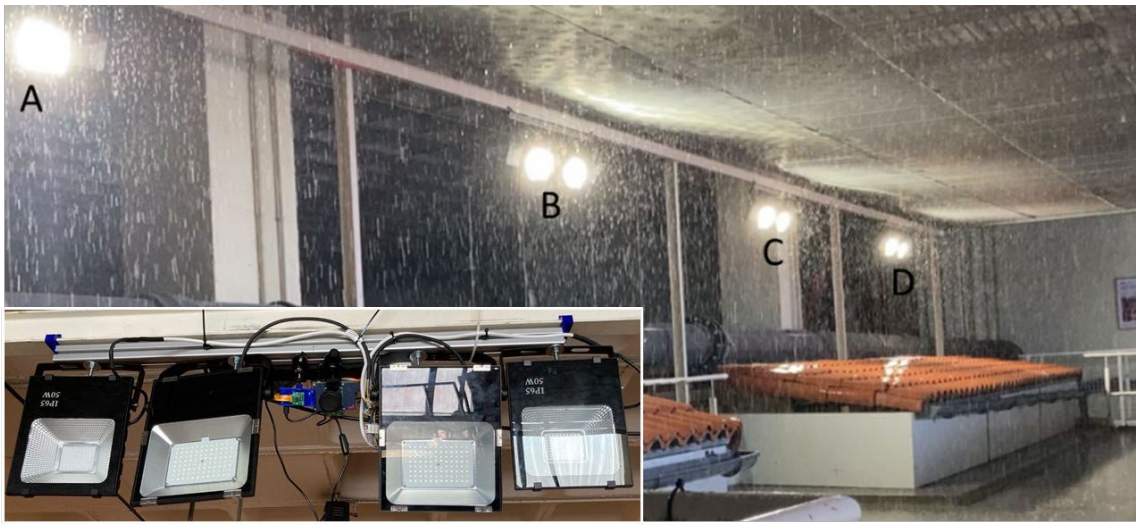

Figure 3.1: Installation of cameras based on Raspberry Pi and lamps in BLOCK. Four positions distributed along the facility was selected to hold two different image acquisition systems and LED and UV lamps.

4.2. LSPIV methodology

Once each camera was pointed to the measurement areas, a rectification of the image is needed. This procedure was carried out by means of a chess pattern carpet. The uniformity of the sizes of the squares means that the coordinates of the squares are known and allows the rectification of the image projection produced by the oblique focus of the cameras to be carried out. This strategy also allows the results obtained in each measurement area to be positioned in a global reference system for the positioning of the results. For this purpose, images are taken from the cameras and the real and pixel coordinates of four points chosen to cover the four corners of the images obtained are determined. These coordinates are used to rectify the obtained frames using the Python library 'OpenCV' as seen in Figure 3.2.

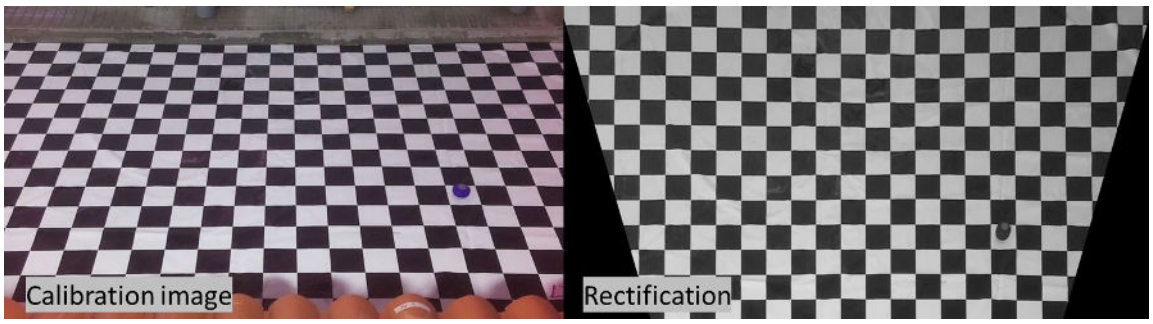

Figure 3.2: Calibration image with the chess pattern carpet disposed over the surface to get the real coordinates to rectify the frames. In addition, the result of the rectification over the calibration image is shown.

The rectified images are then filtered using the Contrast Limited Adaptive Histogram Equalization (CLAHE) image processing technique, a high pass filter and the intensity capping procedure to highlight the particles that will be used as tracers to estimate the surface velocities of the flow. In the tests carried out in this experimental campaign, the tracers used are air bubbles originating naturally from the impact of raindrops on the surface. Figure 3.2 shows an example of original, rectified and filtered frame.

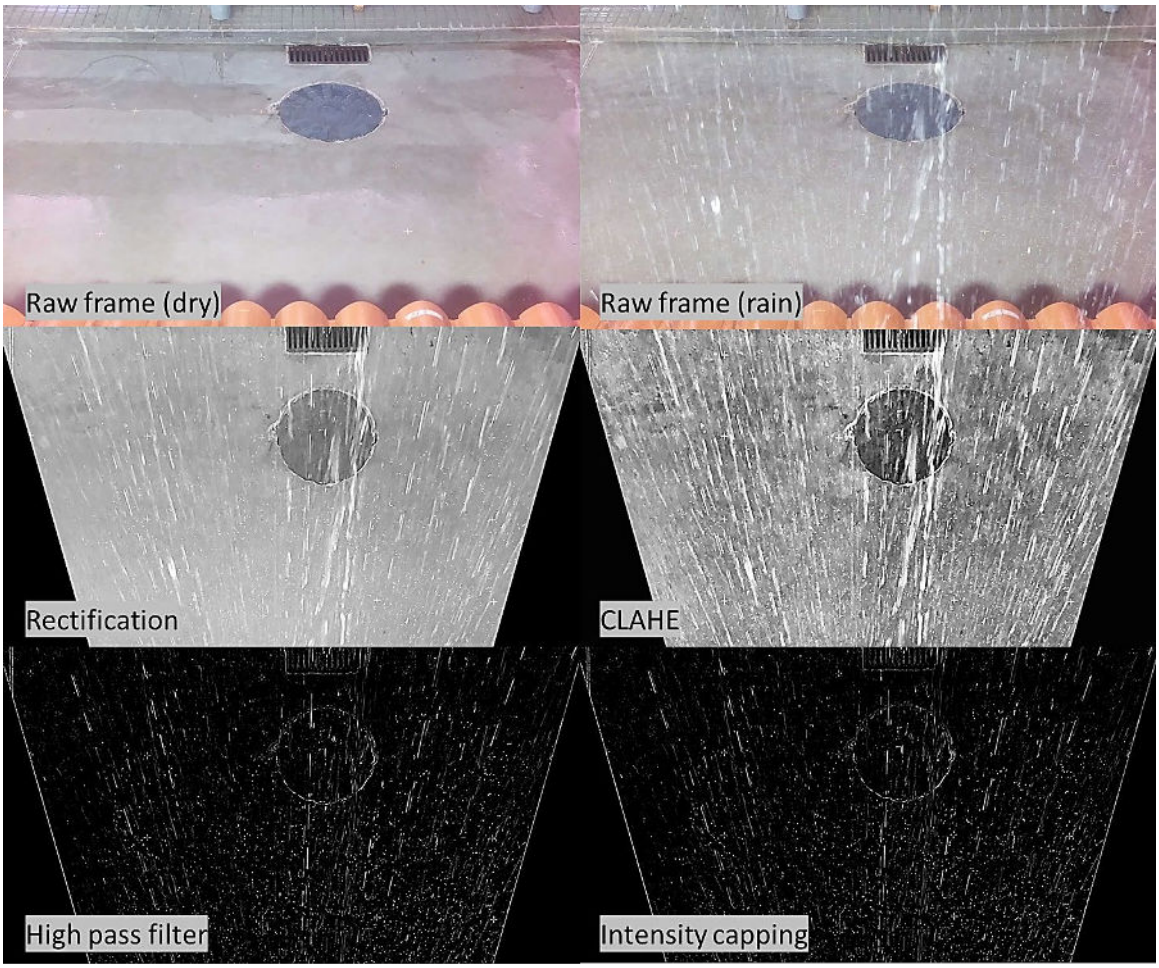

Figure 3.3: Example of the treatment of the frames including rectification of the recording projection, processing and filtering of the images recorded in order to highlight tracers and improve PIV cross-correlation results. The frame corresponds to the camera equipped with a picamera v2 at position A and the H3 experiment.

The open access software OpenPIV was applied to the rectified and filtered frames recorded. The raw velocity results were filtered to remove erroneous vectors using the noise ratio from cross-correlation function, a median spatial filter and a minmax filter. The mean result of 20 consecutive pairs of frames was then obtained considering a median temporal filter. The results are finally scaled, and the reference system is established. Figure 3.3 includes an example of the postprocessing procedure applied where erroneous vectors were removed from raw results.

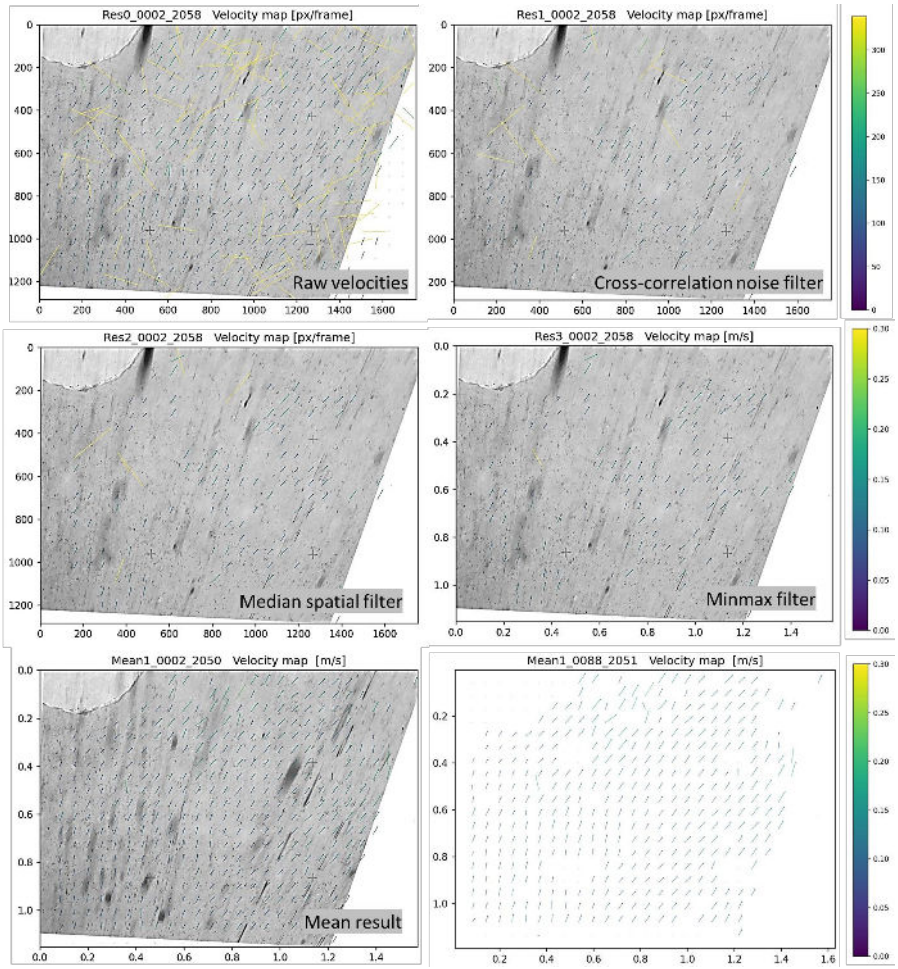

Figure 3.4: Example of postprocessing of raw vectors for H3 test using a raspberry equipped with the HQ camera placed on position A.

4.3. Test procedure

Six different tests were carried out to measure 2D velocities on the surface of the facility (Figure 3.4). First, three constant rain intensities of 30, 50 and 80 mm/h were simulated during 240 s (H1, H2 and H3). This corresponds to steady conditions tests where the three rain intensities that the rainfall simulator can generate were simulated. Then, two intermittent experiments were carried out following Figure 3.4 (H4 and H5) where short periods of rain were generated between gaps of 45 s without rain. During the last experiment the rain intensity was increased and then decreased each 30 s between the available rain intensities (H6). These last experiments pretend to analyse the performance of the methodology for transitory conditions.

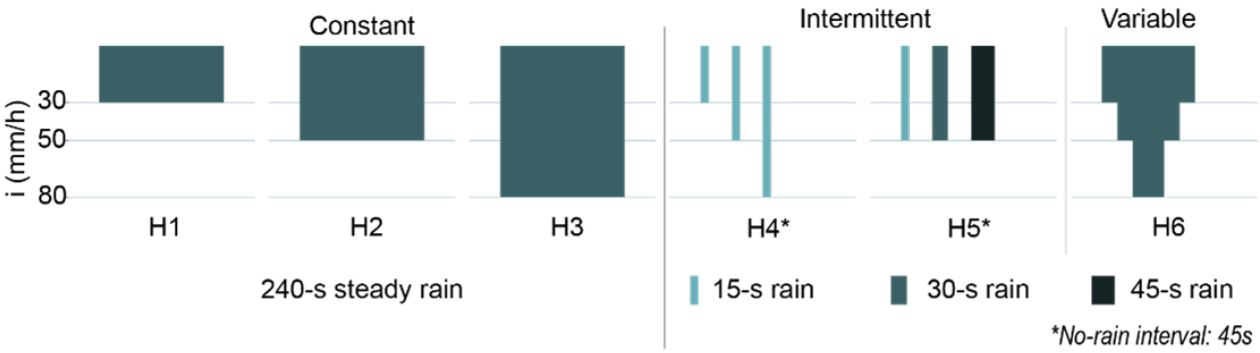

Figure 3.5: Tests carried out during the experimental campaign.

All the cameras were recording frames during the experiments. The acquisition frequency was 10 Hz. A record was kept of the time taken to record each frame, so that possible delays that sometimes occur with the raspberry Zero due to its low processing capacity can be taken into account in the calculation of the velocities. Calibration, preprocessing and postprocessing parameters were optimizing and kept common to all the experiments. Finally, each result is a mean of 20 pair of frames, which is equivalent to 2 s with the 10Hz frequency.

4.4. Results

Figure 3.6 shows an example of processed velocity map obtained in position A using both the picamera and HQ camera configuration during steady conditions of test H2, which corresponds with the constant rain intensity of 50 mm/h. Considering that in the areas corresponding to the manholes covers there is no runoff flow over them (top central part for picamera results and top-left part for HQ camera), the LSPIV methodology is able to properly estimate velocities with a good resolution and in a reliable way, being mean velocities around 0.15 m/s in the studied area. HQ camera allows a higher resolution due the lens used but covering a smaller area.

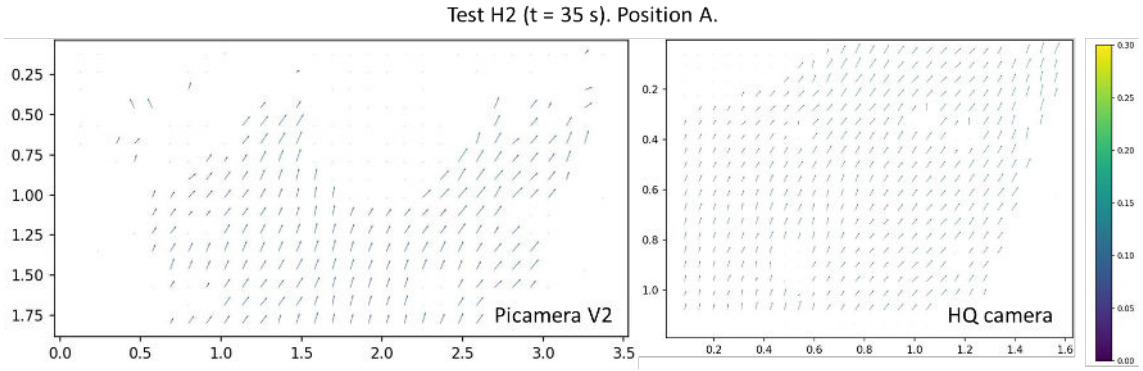

Figure 3.6: Velocity maps obtained in position A using the picamera and HQ camera configuration, respectively. The results correspond to steady conditions of test H2, which corresponds with the constant rain intensity of 50 mm/h.

The results obtained for each camera were also represented in a common reference system and considering all the physical model surface. Figure 3.7 shows the velocity maps obtained from HQ cameras at different times of test H3 corresponding with 5, 15, 71, 201 and 249 s from the start of a constant 80 mm/h 240 s rain. It can be seen how the velocities measurement were increasing towards a stationary point reached before t= 71 s that is kept until the rain stops. Some uncertainty is observed in the first moments of the rain with a small number of vectors and including not valid vectors. The reduction of valid vectors is due reduced flow and the lack of bubbles that are used as tracers, affecting also to the performance of postprocessing filters. Position 2 resulted in higher velocities in stationary results than the rest of positions because the area recorded corresponds with the cross of streets that

the physical model has and thus a larger contributing catchment. This representation of results allows for a better understanding and analysis of the velocities in the full facility and showed the synchronization and calibration of the cameras within the LSPIV methodology developed.

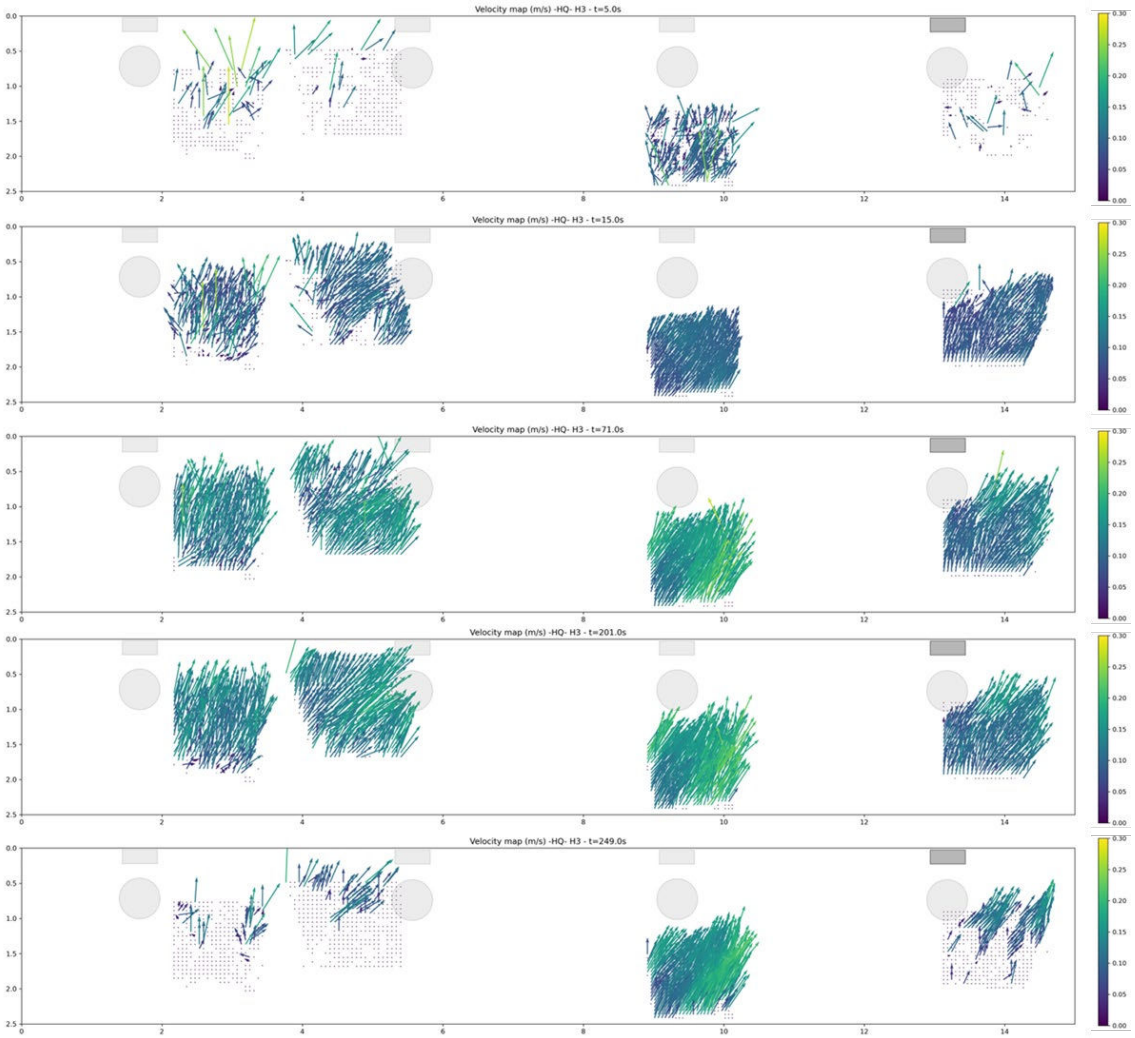

Figure 3.7: Surface velocity maps obtained from HQ cameras at different times of test H3 corresponding with 5, 15, 71, 201 and 249 s from the start of a constant 80 mm/h 240 s rain.

To analyze the temporal variation of the velocities, the mean velocities of an area of 0.3x0.3 m^2 (centered in coordinates X=9.65 m and Y=1.85 m following reference system of Figure 3.7) is represented in Figure 3.8 and Figure 4.9 for all the experiments and cameras. The area corresponds to a common area recorded by picamera and HQ camera from position B. The results for stationary tests (Figure 3.8) demonstrate the reliability of the LSPIV methodology obtaining the same results for the same area recorded by two different cameras with different resolutions. The standard deviations of the vectors within the area considered were represented in the plots, showing an increasing uncertainty with the rain intensity that may due to the presence of more raindrops on the image and also more turbulences produced with their impacts on the water surface. Another issue to highlight is that the camera system consisted of a Raspberry Pi Zero and a picamera V2 was not able to record the frames at 10 Hz because the low processing capabilities of Raspberry Pi Zero, and the irregular timestamps recorded with the images were used for the calculation of velocities. This made the measurement frequency decrease as observed in the plot corresponding picameras, affecting to the estimation of velocities in transient conditions such as the those simulated in tests H4, H5 and H6 (Figure 3.9). Velocity results from picameras also showed a higher uncertainty and

more difficulty to obtain valid vectors at the beginning of the rain. This is due to the larger time differences between consecutive frames and the lower resolution of the tracers in the analysed images.

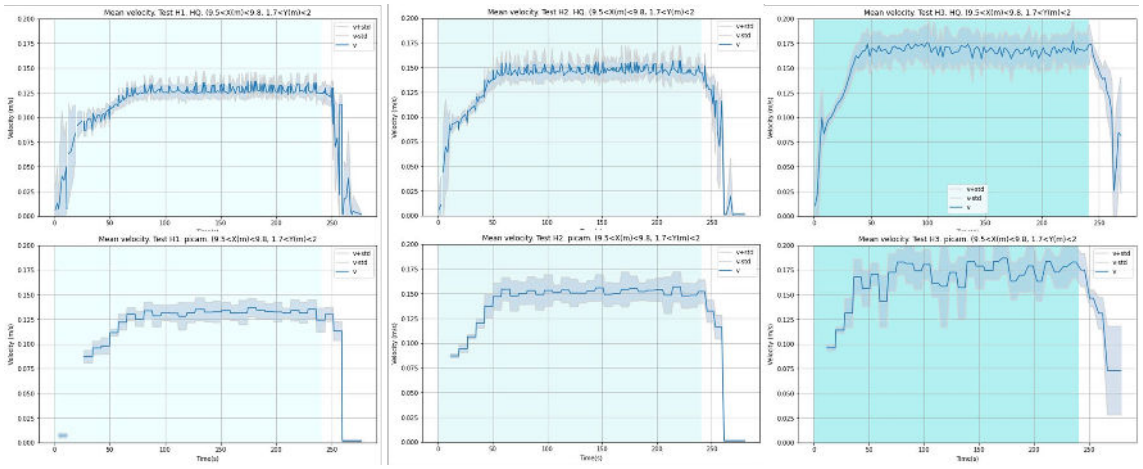

Figure 3.8: Temporal variation of the mean velocities of an area of 0.3x0.3 m² (centered in coordinates X=9.65 m and Y=1.85 m following reference system of Figure 3.7) for HQ camera and picamera for experiments H1, H2, H3, which consist of constant 240 s rains (30,50 and 80 mm/h, respectively).

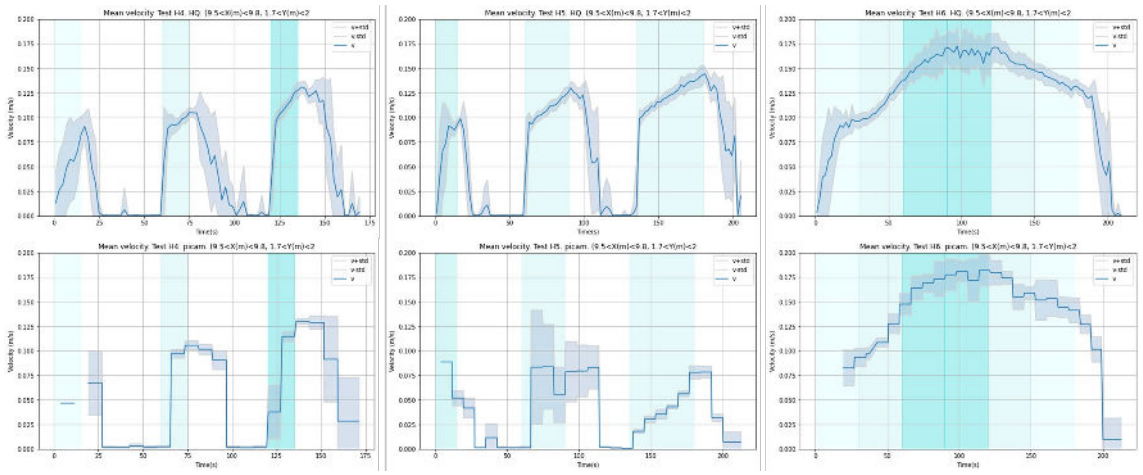

Figure 3.9: Temporal variation of the mean velocities of an area of 0.3x0.3 m² (centered in coordinates X=9.65 m and Y=1.85 m following reference system of Figure 3.7) for HQ camera and picamera for experiments H4, H5, H6.

4.5. Conclusions

A system of low-cost cameras was installed and a LSPIV methodology was developed in the Block facility at the Universidade da Coruña. The LSPIV methodology is able to properly estimate velocities with a good resolution and in a reliable way with the two camera systems installed: i) Raspberry Pi 4 with a HQ camera and ii) Raspberry Pi Zero whit a Picamera V2. The synchronization and calibration of the cameras allow for joining velocity results over the full surface of the facility area. The first camera system resulted in higher spatial and temporal resolution, properly representing stationary and transitory flows with a low uncertainty associated. The picamera V2 of the second camera system considered a much wider area, but the spatial resolution is reduced and the uncertainty in the measurements, specially in case of lack of tracers, increase accordingly. In addition, the Raspberry Pi Zero board reduce the temporal resolution of the results as their processing capabilities limit the frame acquisition rate, affecting to the reliability of transient conditions velocity results. However, the price of the picamera and Raspberry

Pi Zero in comparison to HQ camera and Raspberry Pi 4 (40 as opposed to €140) makes this alternative may also be interesting for certain applications with a high number of cameras and high-resolution results not needed. In sort, the work has highly contributed to improving the capabilities of the facility towards the second call of the Co-UDlabs Transnational programme, complementing the accurate characterization of the hydraulic variables of the experiments to perform in the facility.

5. Investigating geometrical effects on hydraulic energy losses during sewer to surface flow interactions during urban floods.

5.1. Introduction

During urban flood events surcharging drainage systems can interact with surface flows at manholes and gullies (Lee et al., 2019). Excess flow from drainage networks can impact the severity of urban floods, and can also cause a risk to human health (Beg et al., 2020). Hydrodynamic flood modelling tools have developed methodologies to account for such flows. For example, coupled 1D-2D models may simulate pipe flows and surface flows utilising the standard SWE based techniques, with interaction flows between these systems calculated at interaction nodes using semi empirical energy loss equations Djordjević et al., 2005). However, parametrisation of these equations has led to a wide range of reported discharge coefficients/energy loss parameters, with key relationships between energy loss terms and geometrical configurations of the hydraulic structure unexplored (Rubintao et al. 2017). This task will conduct experimental investigations into relationships between energy loss terms and system geometry in a scale model urban drainage system installed at the University of Sheffield.

5.2. Energy Loss Framework

Based on the study of Kitsikoudis et al (2021), during sewer to surface exchange (Figure 4.1) the head losses between the upstream sewer pipe and the surface flow can be described as:

$$H_3 - H_s = \underbrace{\frac{f_{p3} L_3}{D_p} \frac{Q_3^2}{2gA_p^2}}_{\Delta H_1} + \underbrace{k_2 \frac{Q_3^2}{2gA_{pm}^2}}_{\Delta H_2} + \underbrace{\frac{f_m\left(Z_{\text{crest}} - D_p\right)}{D_m} \frac{Q_e^2}{2gA_m^2}}_{\Delta H_3} + \underbrace{k_4 \alpha_4^2 \frac{Q_e^2}{2gA_{ms}^2}}_{\Delta H_4}$$

where *f* is a friction coefficient denoted as *fp3* and *fm* for the upstream sewer pipe and the manhole, respectively. The parameter *α4* is the ratio of flow velocity exiting the manhole to the flow velocity inside the manhole, with *α42* being equal to 0.95 (Idelchik 2007), while the coefficient *k4* is associated with local head losses at the exit of the manhole and is considered equal to 1 (Idelchik 2007). Hence, calibration parameter is the coefficient *k2* associated with head losses due to expansion of the flow from the sewer pipe to the manhole. By rearranging above equation using the standard values of parameters *k4* and *α4*, the numerical value of *k2* can be computed where all required quantities can be evaluated from experimental steady flow observations of *Q3, Hs, H3* and *Qe* taken from the UoS facility.

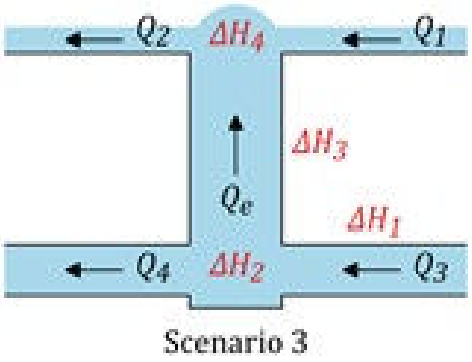

Figure 4.1: Flows and head losses during surcharging pipe/overland flow interaction

When plotting the values of *k2* as a function of the portion of the pipe inflow discharge being exchanged with the surface, *Qe / Q3*, from initial results, conducted with a constant geometry (Kitsikoudis et al. 2021) it appears that

the parameter *k2* varies almost linearly with *Qe / Q3*. Therefore, we consider the following linear function to parameterize *k2*:

$$k_2 = \alpha \frac{Q_e}{Q_3} + \beta$$

Where parameters α and β need to be calibrated with experimental data. Previous experiments from Rubinato et al (2017) where *Am = Ams* and *Ap = Apm = Amp* have given values of α = 0.232 and β = 1.009.

After the calibration of the parameter *k2*, the exchange discharge, *Qe*, in surcharging flow conditions can be estimated through an iterative process by testing values of *Qe* until the two sides of the governing equation converge. The needed input parameters are the flow discharge and pressure in the upstream sewer pipe, the flow discharge on the floodplain (or depth), and the geometric characteristics of the drainage system and the floodplain.

In this work the main contribution is to conduct extensive testing to consider the relationship described in 1 and 2 under conditions which include varying system geometry in addition to flow rates. This will be achieved by fixing different manhole grates at the top of the manhole and re-measuring flow rates and hydraulic energy losses in order to parametrise equation 2 under a range of conditions.

5.3. Experimental setup

This section describes the (I) experimental scale model urban drainage system at UoS system, (II) grate geometries tested in this research and the (III) measured hydraulic conditions for the experimental tests conducted.

5.3.1. Scale model urban drainage system

The experimental tests described here utilise a 1:6 pipe/manhole/surface scale model at the water laboratory at the University of Sheffield (UK). It links a model surface floodplain to an urban drainage system via a manhole shaft (see Figure 4.2). The floodplain surface is 4 m width, 8.2 m length, with a longitudinal slope of 1/1000. Connecting the surface to sewer pipes, the manhole shaft is made from vertical acrylic pipe, has a 0.478 m height, and an inner diameter of 0.24 m. Directly beneath the floodplain, connected by the manhole shaft, is the drainage system made from horizontal acrylic pipes, with an inner diameter of 0.075 m. The facility has been used for a number of previous studies of pipe/surface flow interaction, and more details can be found in, for example, Rubinato et al. (2017).

A pumping system in a closed-circuit supplies water within the facility. With inlet flows to the pipe (*Q3*) and surface (*Q1*) being set independently by automated control valves operated via Labview software. The facility is equipped with a SCADA system (Supervision, Control and Data Acquisition) through Labview software that permits the monitoring and logging of the flow rates and pressure readings within the surface and sewer systems independently.

Pressure sensors (GEMS series 5000) provided the pressure head for upstream of the manhole, in the pipe and on the surface. Sewer pressure sensor is located 350 mm from the centre of the manhole and surface is 460 mm from manhole. The surface downstream outlet is a free outfall. Flow at the sewer outlet can also be controlled by a manual value. Given sufficient flow at *Q3* and applying a restriction to *Q4*, results in net flow exchange from the sewer to the surface (*+ve Qe*).

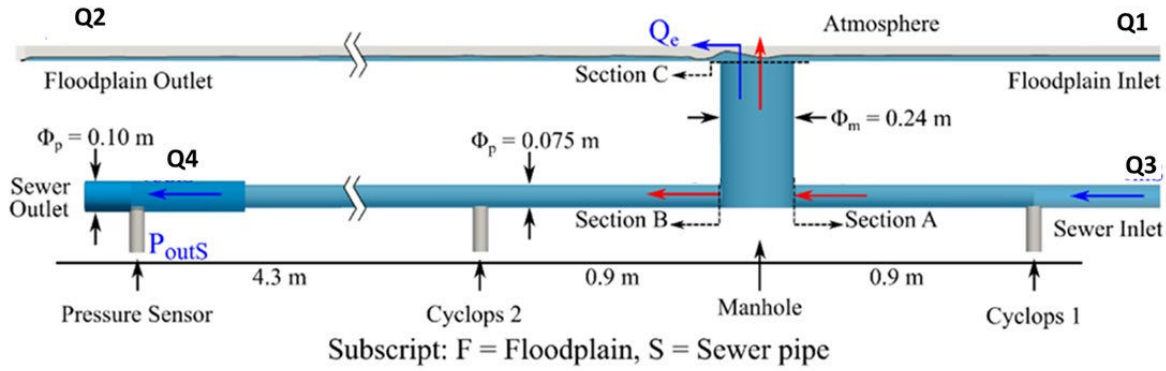

Figure 4.2: Diagram of the A/B rig structure (Beg et al. 2020).

5.3.2. Grate geometry

Six acrylic grates (Figure 4.3), previously constructed for Rubinato et al. (2018) study, were used for these experiments. These were designed in AutoCAD with known geometrical properties, and installed in turn within the urban drainage model (on top of the manhole). For each of these grates, the total area of empty space and total effective edge perimeter length were obtained from the AutoCAD drawings in Rubinato et al. (2018) study and can be found in Table 1.

Table 4.1: Details of the six grates used, from Rubinato et al (2018).

Grate	Area filled (m^2)	Area empty spaces (m^2)	Void ratio (%)	Effective perimeter (m)
1	0.0277	0.0175	38.03	1.8816
2	0.0307	0.0145	32.1	3.0364
3	0.0373	0.0079	17.48	1.3880
4	0.0435	0.0017	3.76	0.5128
5	0.0391	0.0061	13.5	2.2586
6	0.0385	0.0067	14.11	1.2428

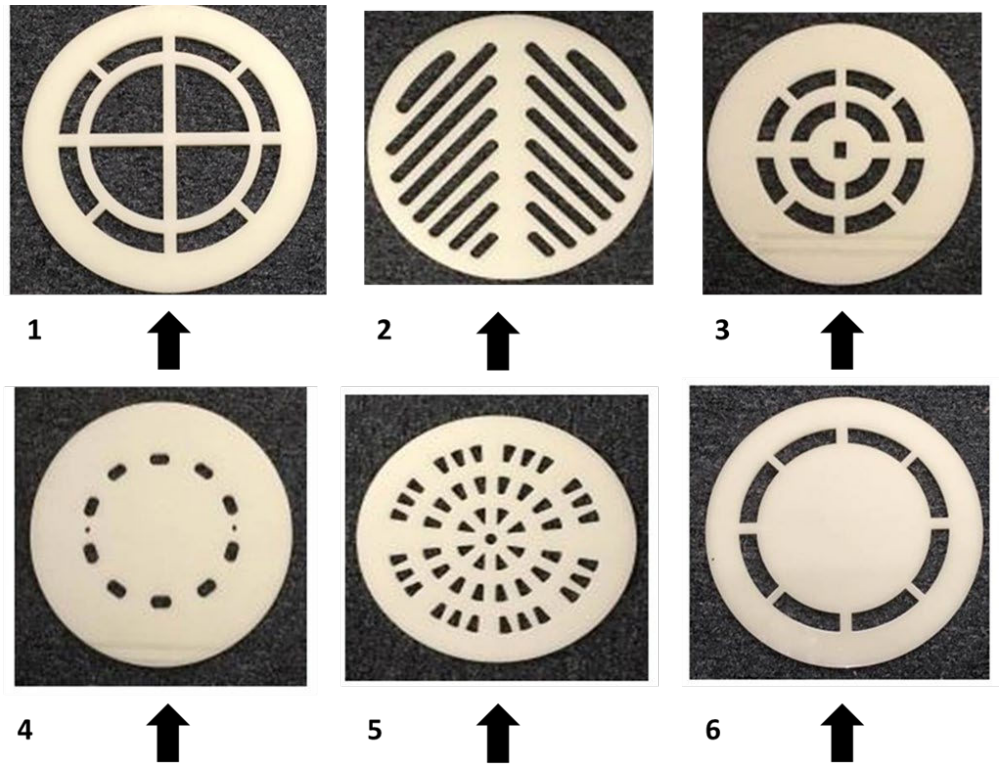

Figure 4.3: Grates applied on top of manhole. Black arrows indicate the orientation of each grate. (Rubinato et al. 2018).

5.3.3. Hydraulic conditions

For each grate, a range of tests were conducted with varying degree of valve restrictions on the downstream sewer pipe (*Q4*) and a range of pipe inflow rates. All tests resulted in net surcharge to the surface (*+ve Qe*). For each test, flow exchange (*Qe*) is quantified by a mass balance established from the surface and sewer inflow and outflows.

As the downstream pipe flow could not be changed/quantified directly; therefore, the upstream valve (*Q3*) was initially set to a flow rate of 10 l/s and the flow in *Q4* was manually restricted five times. This was done by tightening the valve on the downstream pipe until the flowmeter reduced to 9 l/s, 8 l/s, 7 l/s, 6 l/s and 5 l/s: increasing the pressure in the pipe and flow surcharge. Once the downstream pipe was restricted to the chosen variable (i.e., 5 l/s), the upstream valve was set to different flow rates, ranging from 4.5 l/s to 10.6 l/s for the sewer inflows (*Q3*). All tests in this work were conducted in steady flow conditions, this was established by establishing the flow at each setting and recording for an average of 180 seconds to ensure flow stabilisation and full convergence of measured parameters is achieved. In all experiments, the surface flows (*Q1*) were set to 0l/s.

5.4. Results

Time averaged pressure readings and flow exchange values were calculated for each testing condition. Results presented in this section explore the relationship between sewer pipe hydraulic head (*H3*) and flow exchange, as well as resulting energy loss coefficients calculated using equations 1 and 2 based on measured hydraulic and geometrical characteristics. In all cases *H3* and *Hs* are established based on measured pressure and flow velocity (calculated based on flow rate and cross-sectional area). Figure 4.4 plots the measured hydraulic head in the pipe vs flow exchange for all hydraulic conditions and grate types.

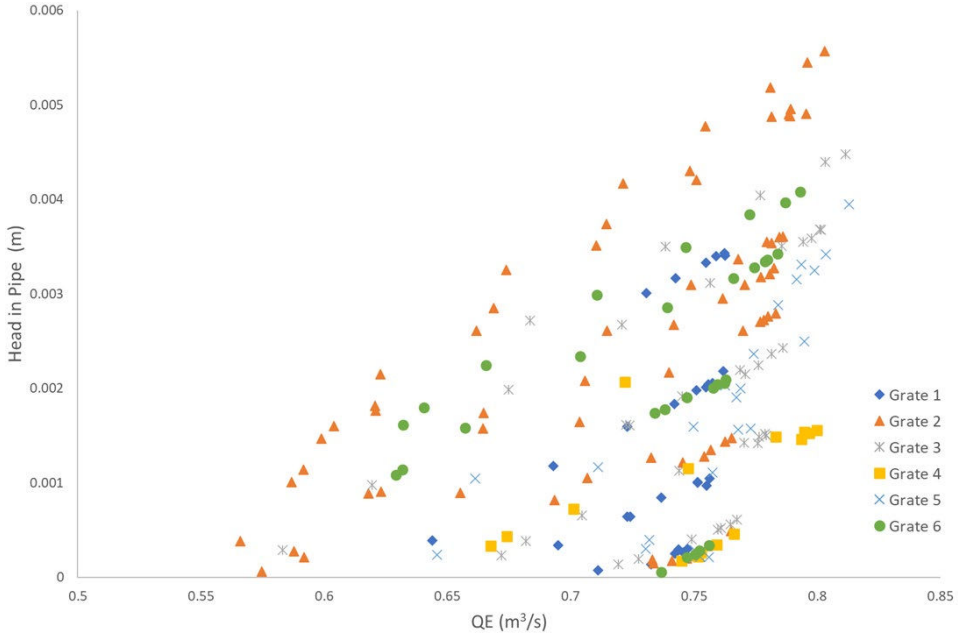

Figure 4.4: Plot of QE against Head in Pipe for all grate types.

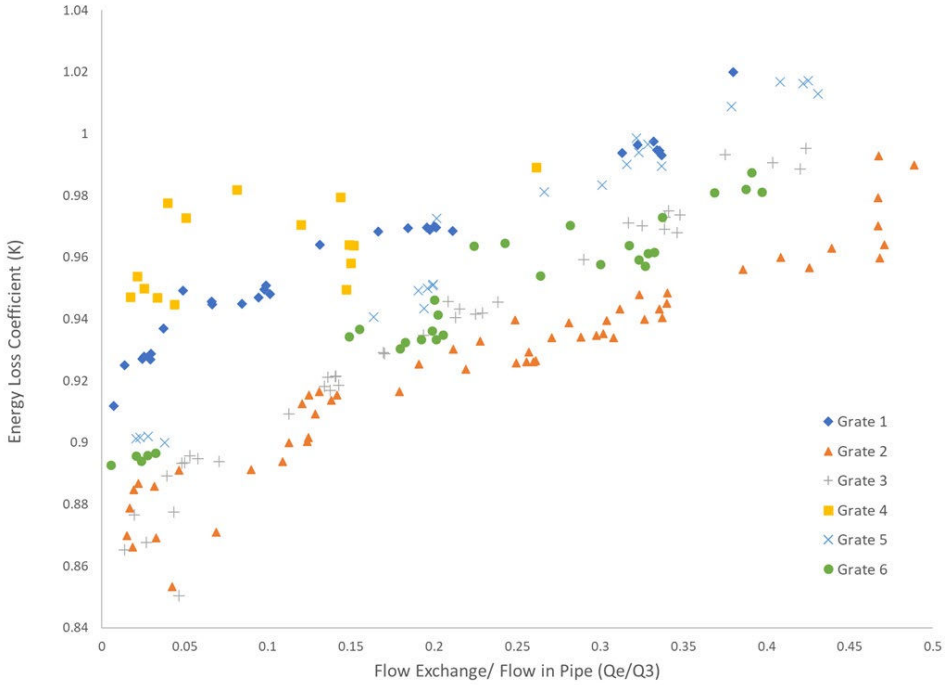

Figure 4.5: Plot of the calculated energy loss coefficient from equation 2, against flow partition (Qe/Q3) for all grate types.

A linear trend for each grate between energy loss coefficient and flow partition can be observed. Similar to Kitsikoudis et al (2021), interrogation of lines or best fit for each grate type provides empirical parameters (α, β) for each grate type. These are presented in table 2, together with lines of best fit.

Table 4.2: Grate characteristics and liner fitting coefficients for each grate.

Grate	Area empty spaces (m^2)	Void ratio (%)	Effective perimeter (m)	α	β	R2
1	0.0175	38.03	1.8816	0.2217	0.9257	0.9566
2	0.0145	32.1	3.0364	0.2281	0.8703	0.8866
3	0.0079	17.48	1.3880	0.3005	0.8728	0.9552
4	0.0017	3.76	0.5128	0.1097	0.9528	0.2843
5	0.0061	13.5	2.2586	0.2968	0.8945	0.9775
6	0.0067	14.11	1.2428	0.2309	0.8928	0.9356

Investigating the linear trend, it appears to display a stable trend, with similar relationships and slope intercepts. Grate 4 has the lowest effective perimeter, which correlates to the lowest alpha and R2 coefficients, but has the highest beta value. Indicating a potential trend of increasing beta with decreasing grate geometry. However, grate 1, with the highest effective perimeter, possesses the second-highest beta value, contradicting the pattern of increasing beta with decreasing geometry.

Overall analysis suggests a potential, if not, complex relationship between effective perimeter and beta for the different grate geometries. As grate 4 deviates from the expected relationship displayed in the other grates, such as grate 1 and grate 3. The other grates all follow consistent trends despite their varying parameters. Therefore, further investigation is required to understand the underlying influences of these observed trends.

5.5. Conclusion

This work has investigated the relationship between grate geometry and hydraulic energy loss coefficients in urban flood conditions. Results have shown that the general energy loss framework presented in Kitsikoudis et al (2021) can be applied over a range of system geometries, with alinaer trend between energy loss coefficients and flow partition at the manhole. Future work will explore the greater range of hydraulic flows on surface and unsteady flow conditions.

6. Conclusions and contribution towards the objectives of Co-UDlabs

The recent technologies based on the acquisition and processing of optical and laser images offer new possibilities to characterise and analyse the hydrodynamic performance of urban drainage systems.

We have shown that techniques as LIDAR (Laser Imaging Detection and Ranging), SfM (Structure from Motion) and depth cameras can be used to represent the geometry of urban systems with a much high accuracy and resolution than conventional topography techniques. SfM and LIDAR have proven specially performing, since they are able to detect small variations in the surface, in the order of millimeters. An additional advantage of these techniques, especially of SfM, is the relatively low cost, resulting in an optimal solution for obtaining a high-resolution and accurate elevation map in large-scale facilities.

A revision on the application of imaging techniques to urban drainage is in process involving most of the Co-UDlabs partners. This revision discusses the growing importance of these techniques, fostered by the emergence of affordable hardware, deep learning developments for image processing and open-source software. It also explores in detail various specific applications relevant to the UD community including flow measurement, infrastructure mapping and water quality, and discusses the developments most urgently required in the field from a technical and organizational perspective.

Optical imaging techniques have also proven very useful to register the water velocity in very shallow flows. We have developed a methodology to apply LSPIV (Large Scale Particle Image Velocimetry) to the estimation of water velocity in very shallow flows (surface runoff). While LSPIV is currently commonly used in hydraulics, its application to urban drainage is much scarcer due to additional complexities in the treatment of images steaming from the shallowness of the flow and the impact of raindrops in the surface. We have developed a low-cost methodology to apply LSPIV to this kind of conditions, opening up the possibility to measure surface runoff velocity in large scale facilities with a high spatial and temporal resolution.

It is worth noting that the techniques and methodologies developed within this task will contribute to improving the capabilities of the laboratory facilities offered by University of A Coruña in the second call of the Co-UDlabs Transnational programme, complementing the accurate characterization of the hydraulic variables of the experiments to perform in the facility.

Finally, the relationship between grate geometry and hydraulic energy loss coefficients in urban flood conditions was investigated in a dedicated specific task to improving the current characterization of these kind of flooding. Further work will explore the greater range of hydraulic flows on surface and unsteady flow conditions.

7. References

Beg, M.N.A., Rubinato, M., Carvalho, R.F. and Shucksmith, J.D., 2020. CFD modelling of the transport of soluble pollutants from sewer networks to surface flows during urban flood events. Water, 12(9), p.2514.

Bradski, G. (2000). The openCV library. Dr. Dobb's Journal: Software Tools for the Professional Programmer, 25(11), 120-123.

Djordjević, S., Prodanović, D., Maksimović, Č., Ivetić, M., & Savić, D. (2005). SIPSON–Simulation of Interaction between Pipe flow and Surface Overland flow in Networks. Water Science and Technology, 52(5), 275-283.

Idelchik, I. E. 2007. Handbook of Hydraulic Resistance. (A. S. Ginevskiy and A. V. Kolesnikov, Eds.), 4th edition. Begell House, translated by G. R. Malyavska.

Kitsikoudis et al 2021 Exchange between drainage systems and surface flows during urban flooding: Quasi-steady and dynamic modelling in unsteady flow conditions, Journal of Hydrology, 602: 126628 https://doi.org/10.1016/j.jhydrol.2021.126628.

Lee, S., & An, H. (2019). Evaluating the effect of grid size and type in integrated 1D/2D coupled urban inundation modelling on the interacting discharge between the surface and sewerage system. Journal of Flood Risk Management, 12, e12537.

Liberzon, A, Lasagna, D, Aubert, M, Bachant, P, Käufer, T, Bauer, A, Vodenicharski, B, Dallas, C, Borg, J, tomerast & ranleu. (2020). OpenPIV/openpiv-python: OpenPIV - Python (v0.22.2) with a new extended search PIV grid option (0.22.2). Zenodo. https://doi.org/10.5281/zenodo.3930343

Rubinato, M., Martins, R., Kesserwani, G., Leandro, J., Djordjević, S., & Shucksmith, J. (2017). Experimental calibration and validation of sewer/surface flow exchange equations in steady and unsteady flow conditions. Journal of hydrology, 552, 421-432.

Rubinato, M., S. Lee, R. Martins, and J. D. Shucksmith. 2018a. Surface to sewer flow exchange through circular inlets during urban flood conditions. J. Hydroinf. 20:564–576.